

A computational fluid dynamics of ‘clap and fling’ in the smallest insects

Laura A. Miller^{1,*} and Charles S. Peskin²

¹*Department of Mathematics, University of Utah, 155 South 1400 East, Salt Lake City, UT 84112, USA and*
²*Courant Institute of Mathematical Sciences, New York University, 251 Mercer Street, New York, NY 10012, USA*

*Author for correspondence (e-mail: miller@math.utah.edu)

Accepted 8 November 2004

Summary

In this paper, we have used the immersed boundary method to solve the two-dimensional Navier–Stokes equations for two immersed wings performing an idealized ‘clap and fling’ stroke and a ‘fling’ half-stroke. We calculated lift coefficients as functions of time per wing for a range of Reynolds numbers (Re) between 8 and 128. We also calculated the instantaneous streamlines around each wing throughout the stroke cycle and related the changes in lift to the relative strength and position of the leading and trailing edge vortices.

Our results show that lift generation per wing during the ‘clap and fling’ of two wings when compared to the average lift produced by one wing with the same motion falls into two distinct patterns. For $Re=64$ and higher, lift is initially enhanced during the rotation of two wings when lift coefficients are compared to the case of one wing. Lift coefficients after fling and during the translational part of the stroke oscillate as the leading and trailing edge vortices are alternately shed. In addition, the lift coefficients are not substantially greater in the two-winged case than in the one-winged case. This differs from three-

dimensional insect flight where the leading edge vortices remain attached to the wing throughout each half-stroke. For $Re=32$ and lower, lift coefficients per wing are also enhanced during wing rotation when compared to the case of one wing rotating with the same motion. Remarkably, lift coefficients following two-winged fling during the translational phase are also enhanced when compared to the one-winged case. Indeed, they begin about 70% higher than the one-winged case during pure translation. When averaged over the entire *translational* part of the stroke, lift coefficients per wing are 35% higher for the two-winged case during a 4.5 chord translation following fling. In addition, lift enhancement increases with decreasing Re . This result suggests that the Weis-Fogh mechanism of lift generation has greater benefit to insects flying at lower Re . Drag coefficients produced during fling are also substantially higher for the two-winged case than the one-winged case, particularly at lower Re .

Key words: insect flight, Reynolds number, aerodynamics, computational fluid dynamics, clap and fling.

Introduction

While analyzing the hovering motion of the tiny wasp *Encarsaria formosa*, Weis-Fogh (1973) proposed a novel aerodynamic mechanism that enhanced lift during flight. This mechanism became known as the Weis-Fogh mechanism, and the corresponding motion has been termed ‘clap and fling’. Lighthill (1973) described analytically how this motion is thought to augment lift using two-dimensional inviscid theory. Later studies revealed that clap and fling is also used by insects such as the greenhouse white-fly *Trialeurodes vaporariorum* (Weis-Fogh, 1975), thrips (Ellington, 1984) and butterflies (Srygley and Thomas, 2002). Although most, if not all, tiny insects use ‘clap and fling’, the majority of insects do not (Ellington, 1999). Moreover, clap and fling could be merely a result of the insect maximizing stroke amplitude rather than an independently evolved behavior to maximize lift. As a result, clap and fling is not considered a general method of lift generation in insect flight. There has not, however, been a

rigorous study comparing the effects of ‘clap and fling’ for different Reynolds numbers (Re). It is not known, therefore, if the lift-enhancing effects of clap and fling are greater for the smallest insects in comparison to larger insects.

During clap and fling, the wings ‘clap’ together at the end of the upstroke (ventral to dorsal) and then fling apart at the beginning of the downstroke (dorsal to ventral). The tiny wasp *Encarsaria formosa* and presumably other tiny insects fly with their bodies inclined almost vertically (Weis-Fogh, 1973). The wings are translated back and forth along a nearly horizontal plane (Fig. 1A). At the beginning of the downstroke, the wings initially fling apart by rotating about the common trailing edge (Fig. 1B). During this rotation, large attached leading edge vortices form on each wing (Maxworthy, 1979; Spedding and Maxworthy, 1986). The leading edge vortex of one wing acts as the starting vortex of the other wing. Since these vortices are mirror images of each other, the circulation about the pair

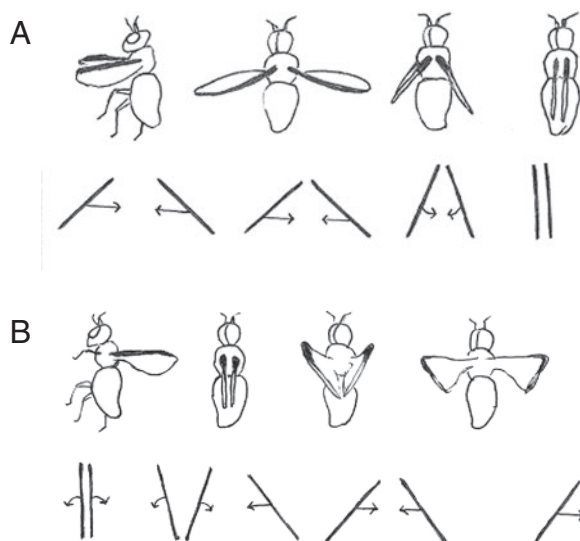


Fig. 1. 'Clap and fling' (redrawn from Weis-Fogh, 1973). The three-dimensional motion (top) and the corresponding two-dimensional approximation (bottom). In this drawing, the insect flies with its body oriented almost vertically, and the wings move in a horizontal plane. At the beginning of the upstroke (A), the wings move from the ventral to the dorsal side of the body, and rotate together about the leading edges. At the beginning of the downstroke (B), the wings rotate apart about the trailing edges. Towards the end of rotation, the wings translate away from each other.

of wings remains zero. As a result, trailing edge vortices are not needed to conserve circulation, and indeed they are not initially formed. This is significant because both leading and trailing edge vortices are formed by a single wing in pure translation, resulting in smaller lift forces. This vortical pattern leads to larger lift forces when compared to similar wing kinematics without clap and fling (Lighthill, 1973; Sun and Yu, 2003). Towards the end of rotation, the two wings begin to translate away from each other along a horizontal plane.

The Weis-Fogh mechanism of lift generation has been verified by a number of experimental and computational studies. Maxworthy (1979) confirmed the basic premise of the Weis-Fogh mechanism using flow visualization on model wings. Essentially, this study showed that two large leading edge vortices are formed during fling. However, his results showed that the magnitude of the circulation about each wing generated during fling is much larger than that predicted by Lighthill. This result was also confirmed by Haussling (1979) who determined the instantaneous streamlines and vorticity lines by solving numerically the full Navier–Stokes equations. Spedding and Maxworthy (1986) measured the instantaneous lift forces on model wings during fling and found that the forces were larger than those predicted by Lighthill. Sunada et al. (1993) characterized the effects of 'near fling' on lift generation using a series of three-dimensional experiments. Near fling describes the case where the wings are only partially clapped together. Using computational fluid dynamics, Sun and Yu (2003) found that lift is also enhanced for some time

during the translational phase of the stroke following a simple fling at $Re=17$. They did not, however, consider this effect for different Re .

There is reason to believe that the lift enhancing effects of the Weis-Fogh mechanism could increase with decreasing Re . Using two-dimensional computational fluid dynamics, we have determined that the lift coefficients generated during translation are lower for $Re<32$ than for $Re>64$ (Miller and Peskin, 2004). Wu and Sun (2004) also found that lift coefficients were greatly reduced for $Re<100$ in three-dimensional simulations without clap and fling. This drop in lift corresponds to a change in the behavior of the vortex wake. For $Re=64$ and above, a leading edge vortex is formed and at least initially remains attached to the wing. The trailing edge vortex is formed and shed from the wing. The stability of the attached leading edge vortex appears to vary with several factors, one of which is the dimensionality of the flow. In two dimensions, leading and trailing edge vortices are alternately shed forming the von Karman vortex street (Dickinson and Götz, 1993; Birch et al., 2004; Miller and Peskin, 2004). The real situation of insect flight differs from the two-dimensional model in at least two ways: the insect wing has finite span, and its motion involves rotation about the dorsal–ventral axis of the insect. In the three-dimensional rotating motion, the leading edge vortex appears to remain attached for all time (Usherwood and Ellington, 2002). Birch et al. (2004) also observed a stable attached leading edge vortex for $Re=120$ and $Re=1400$ using a dynamically scaled robotic insect. For $Re=32$ and below, both leading and trailing edge vortices are formed and remain attached to the wing (Miller and Peskin, 2004), and the leading edge vortex is more diffuse than the higher Re case (Wu and Sun, 2004). The drop in lift for lower Re is related to a loss of asymmetry in the vortical pattern behind the wing. A similar transition has been observed for thrust generation in flapping flight (Childress and Dudley, 2004; Vandenberghe et al., 2004).

For these lower Re (32 and below), lift might be enhanced during translation by 'regaining' vortical asymmetry through clap and fling. In the case of pure translation, equally sized leading and trailing edge vortices (by the principle of conservation of vorticity) are formed at the beginning of the stroke and remain attached to the wing until stroke reversal. During clap and fling, two equally sized large leading edge vortices are formed, and no trailing edge vortices are formed initially. Presumably, trailing edge vortices will form and grow in strength during translation, reaching the same strength as the leading edge vortices after a sufficient amount of time. However, transient asymmetry between the leading and trailing edge vortices should be produced by fling. This asymmetry in the vortical field should lead to larger lift forces than in the case of pure translation.

In this paper, a two-dimensional version of clap and fling is studied for Re ranging from 8 to 128, using the immersed boundary method. Two motions are considered: 'clap' and 'fling'. Clap was modeled as a motion similar to that of Fig. 1A, and was divided into three stages: acceleration from

rest at constant angle of attack, translation, and rotation about the leading edge. Fling was modeled as a motion similar to that of Fig. 1B, and was divided into two stages: rotation about the trailing edge and translation. The first set of simulations corresponds to fling and the downstroke. The second set of simulations corresponds to the upstroke, clap, fling, and the subsequent downstroke. The lift forces generated *per wing* for each Re were compared to the lift forces generated in the case of one wing moving with the same motion.

Materials and methods

The basic design of this study is similar to that of our previous computational work (Miller and Peskin, 2004), which was modeled after a physical experiment of Dickinson and Götz (1993). In this particular experiment, Dickinson and Götz immersed a robotic wing in sucrose solution to study flight dynamics similar to that of *Drosophila melanogaster*. This experiment was dynamically scaled such that the Re of the model was approximately equal to that of *Drosophila melanogaster* flight. The Re basically describes the ratio of inertial to viscous forces in fluid flow and is given by the equation:

$$Re = \frac{\rho l U}{\mu} = \frac{l U}{\nu}, \quad (1)$$

where ρ is the density of the fluid, μ is the dynamic viscosity of the fluid, ν is the kinematic viscosity of the fluid, l is a characteristic length of the immersed structure, and U is a characteristic velocity of the flow. In our case, l is the chord length of the wing (c), and U is the velocity of the wing during the translational phase of the motion. The parameters in our computational study were chosen to match those of the Dickinson and Götz experiment, except that we varied the velocity of the wing to change the Re . Their experiment used an aluminum wing with a chord of 5 cm immersed in a sucrose solution with a dynamic viscosity of 0.0235 N s m⁻², about 20 times that of water. The two dimensions of the experimental tank relevant to our two-dimensional simulations were 1 m in length \times 0.4 m in width. In our simulations, the size of the computational fluid domain was increased to 1 m in length \times 1 m in width. This was done to reduce wall effects, which become more significant at lower Re .

The full ‘clap and fling’ motion studied here is a two-dimensional idealization of one complete three-dimensional stroke. The wings are translated towards each other from rest at a constant angle of attack during the initial translational phase. Near the end of this initial half-stroke, the wings rotate along the leading (upper) edge and are nearly clapped together. A distance of 1/6 chord lengths is left between the wings, however. This half-stroke is called the upstroke since its three-dimensional counterpart describes the motion of the wing from the ventral to the dorsal side of the body. At the beginning of the downstroke, the wings are held parallel and then rotated apart about the trailing (lower) edge. By convention, the downstroke is defined as the motion of the

wing from the dorsal to the ventral side of the body. The translational phase of the motion, which begins towards the end of the rotational phase, is defined as the translation of the wings away from each other along the horizontal axis. In a three-dimensional version of this simulation, the translational phase would correspond to the motion of the wings from the dorsal to the ventral side of the body. In the case of ‘fling’ (downstroke only) the wings translate through a distance of about 4.5 chord lengths. In the case of ‘clap and fling’ (one entire stroke) the wings translate through a distance of about 3.5 chord lengths.

At present, no detailed quantitative description of the clap and fling motion in small insects is available in the literature. Therefore, a ‘reasonable’ fling motion was constructed based on the normalized angular velocities and translational accelerations used to model the flight of *Drosophila melanogaster*. To construct a smooth motion with positive lift generated throughout the stroke, wing rotation began before wing translation ended during the upstroke. This motion was constructed such that translation ended halfway through the first rotational phase. The wings were rotated at the end of the upstroke about the leading edges (clap). At the beginning of the downstroke, the wings were rotated apart about the trailing edges (fling). The translational phase of the downstroke also began halfway through the second rotational phase.

The kinematics of the left wing are described here. The right wing (when present) was the mirror image of the left wing at all times during its motion. The translational velocities over time were constructed with a set of equations describing the acceleration and deceleration phases of wing translation (Fig. 2). The translational velocity during the acceleration phases of the wing is given by:

$$v(\tau) = \frac{1}{2} V \left\{ 1 + \cos \left[\pi + \frac{\pi(\tau - \tau_{\text{accel}})}{\Delta\tau_{\text{accel}}} \right] \right\}, \quad (2)$$

$$\tau = tV/c, \quad (3)$$

where V is the maximum translational velocity during the stroke, $v(\tau)$ is the translational velocity at dimensionless time τ defined by Eq. 3, t is the actual time, c is the chord length of the wing, τ_{accel} is the dimensionless time when translational acceleration begins, and $\Delta\tau_{\text{accel}}$ is the dimensionless duration of translational acceleration. After acceleration, the translational velocity of the wing is fixed as V . The translational velocities during deceleration are given as:

$$v(\tau) = V - \frac{1}{2} V \left\{ 1 + \cos \left[\pi + \frac{\pi(\tau - \tau_{\text{decel}})}{\Delta\tau_{\text{decel}}} \right] \right\}, \quad (4)$$

where τ_{decel} is the dimensionless time when translational deceleration begins, and $\Delta\tau_{\text{decel}}$ is the dimensionless duration of translational deceleration. In these simulations, the dimensionless duration of an entire clap and fling stroke was taken to be 10.8 (this gives a translational distance of about 3.5 chord lengths). The dimensionless duration of a fling half-

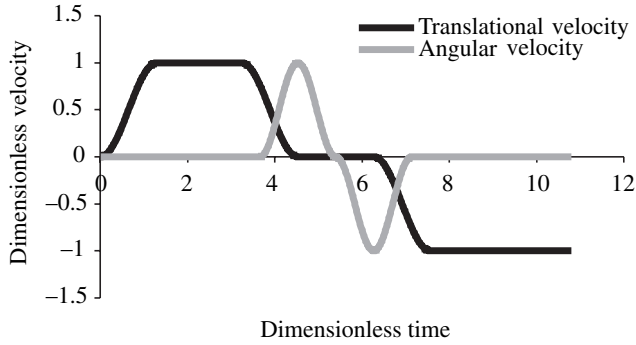


Fig. 2. Dimensionless translational and angular velocities of the wing as a function of dimensionless time for one ‘clap and fling’ stroke. The total motion was used for all ‘clap and fling’ simulations. For ‘fling’ simulations, the angular and translational velocities follow the second half of the graph. Note that the wing begins to rotate before the end of translation during the upstroke (first half-stroke). Translation during the downstroke (second half-stroke) also begins before wing rotation has ended.

stroke was taken to be 6 (this gives a translational distance of about 4.5 chord lengths), τ_{accel} and τ_{decel} were taken to be 0.86, $\Delta\tau_{\text{accel}}$ and $\Delta\tau_{\text{decel}}$ were taken to be 1.3, and V ranged from about 0.00375 to 0.06 m s^{-1} .

The angles of attack were similarly defined using a set of equations describing the angular velocity during the rotational phase of the stroke. Let α be defined as the angle of attack of the wing relative to the horizontal plane. In all fling simulations, the wings were rotated from $\alpha=90^\circ$ to $\alpha=45^\circ$ at the beginning of the downstroke. After rotation, the angle of attack was held constant for the remainder of the stroke. In all clap and fling simulations, the wings were translated at constant angle of attack of 45° during the upstroke and rotated to 90° at the end of the upstroke. The downstroke was constructed exactly as the fling case. Let θ be defined as the angle between the left wing and the positive x -axis (the origin is defined as the intersection of the wing with the x -axis at the initial time). The angular velocity of the left wing during the rotational phase at the end of the upstroke is given by:

$$\omega(\tau) = \frac{1}{2} \omega_{\text{rot}} \left\{ 1 - \left(\cos \left[2\pi \frac{\tau - \tau_{\text{turn}}}{\Delta\tau_{\text{rot}}} \right] \right) \right\} \quad (5)$$

and

$$\omega_{\text{rot}} = \frac{2\Delta\theta V}{\Delta\tau_{\text{rot}} c}, \quad (6)$$

where ω_{rot} is a constant determined by the total angle of rotation and by the duration of the rotational phase in Eq. 6, $\omega(\tau)$ is the angular velocity as a function of dimensionless time, τ_{turn} is the dimensionless time wing rotation begins, $\Delta\tau_{\text{rot}}$ is the dimensionless duration of the rotational phase, and $\Delta\theta$ is the total angle through which rotation occurs. Unless otherwise noted, $\Delta\theta$ was set to $\pi/4$ and $\Delta\tau_{\text{rot}}$ was set to 1.74 in all

simulations. Rotation at the beginning of the downstroke was constructed similarly.

The numerical method

For the simulations presented here, a ‘target boundary’ version of the immersed boundary method was used to calculate the flow around the wing. Basically, we wanted the wing to move with small deformations in a prescribed motion. To achieve this, a target boundary that does not interact with the fluid is attached with virtual springs to the actual immersed boundary. This target boundary moves with the desired motion, and the spring attachments apply a force to the actual boundary which is proportional to the distance between corresponding points of the two boundaries. In other words, an external force is applied that is proportional to the distance between the wing and its desired trajectory. The force applied to the actual immersed boundary by the target boundary and the deformation of the actual boundary are then used to calculate the force applied to the fluid.

The two-dimensional incompressible Navier–Stokes equations describing the motion of the fluid are as follows:

$$\rho \left(\frac{\partial \mathbf{u}(\mathbf{x}, t)}{\partial t} + \mathbf{u}(\mathbf{x}, t) \cdot \nabla \mathbf{u}(\mathbf{x}, t) \right) = -\nabla P(\mathbf{x}, t) + \mu \Delta \mathbf{u}(\mathbf{x}, t) + \mathbf{F}(\mathbf{x}, t) \quad (7)$$

and

$$\nabla \cdot \mathbf{u}(\mathbf{x}, t) = 0, \quad (8)$$

where $\mathbf{u}(\mathbf{x}, t)$ is the fluid velocity, $P(\mathbf{x}, t)$ is the pressure, $\mathbf{F}(\mathbf{x}, t)$ is the force per unit area applied to the fluid by the immersed wing, ρ is the density of the fluid, and μ is the dynamic viscosity of the fluid. The independent variables are the time t and the position vector $\mathbf{x}=[x, y]$. Note that bold letters represent vector quantities.

The interactions between the fluid and the boundary are described by the following equations:

$$\mathbf{F}(\mathbf{x}, t) = \int \mathbf{f}(r, t) \delta[\mathbf{x} - \mathbf{X}(r, t)] dr \quad (9)$$

and

$$\frac{\partial \mathbf{X}(r, t)}{\partial t} = \mathbf{U}[\mathbf{X}(r, t)] = \int \mathbf{u}(\mathbf{x}, t) \delta[\mathbf{x} - \mathbf{X}(r, t)] d\mathbf{x}, \quad (10)$$

where $\mathbf{f}(r, t)$ is the force per unit length applied by the wing to the fluid as a function of Lagrangian position (r) and time (t), $\delta(\mathbf{x})$ is a two-dimensional delta function, $\mathbf{X}(r, t)$ gives the Cartesian coordinates at time t of the material point labeled by the Lagrangian parameter r . Eq. 9 describes how the force is spread from the boundary to the fluid. Eq. 10 evaluates the local velocity of the fluid at the boundary. In this numerical scheme, the boundary is moved at the local fluid velocity at each time step, and this enforces the no-slip condition. Each of these equations involves a two-dimensional Dirac delta function δ , which acts in each case as the kernel of an integral transformation. These equations convert Lagrangian variables to Eulerian variables and *vice versa*.

The equations that describe the force the boundary applies to the fluid are given as:

$$\mathbf{f}_{\text{targ}}(r,t) = k_{\text{targ}}[\mathbf{Y}(r,t) - \mathbf{X}(r,t)] + c_{\text{targ}} \left(\frac{\partial \mathbf{Y}(r,t)}{\partial t} - \frac{\partial \mathbf{X}(r,t)}{\partial t} \right), \quad (11)$$

$$\mathbf{f}_{\text{beam}}(r,t) = -k_{\text{beam}} \frac{\partial^4 \mathbf{X}(r,t)}{\partial r^4}, \quad (12)$$

$$\mathbf{f}_{\text{str}}(r,t) = k_{\text{str}} \frac{\partial}{\partial r} \left[\left(\left| \frac{\partial \mathbf{X}}{\partial r} \right| - 1 \right) \frac{\partial \mathbf{X}(r,t)/\partial r}{\left| \partial \mathbf{X}(r,t)/\partial r \right|} \right], \quad (13)$$

and

$$\mathbf{f}(r,t) = \mathbf{f}_{\text{targ}}(r,t) + \mathbf{f}_{\text{beam}}(r,t) + \mathbf{f}_{\text{str}}(r,t). \quad (14)$$

Eq. 11 describes the external force applied to the fluid that is proportional to the distance between the boundary and its desired trajectory. $\mathbf{f}_{\text{targ}}(r,t)$ is the force per unit length, k_{targ} is a stiffness coefficient, c_{targ} is a damping coefficient, and $\mathbf{Y}(r,t)$ is the prescribed position of the target boundary. Eq. 12 describes the force applied to the fluid by the boundary as a result of its elastic deformation in bending. $\mathbf{f}_{\text{beam}}(r,t)$ is the force per unit length and k_{beam} is a stiffness coefficient. Eq. 13 describes the force applied to the fluid as a result of the resistance to stretching of the boundary [$\mathbf{f}_{\text{str}}(r,t)$]. k_{str} is the corresponding stiffness coefficient in tension or compression. Finally, Eq. 14 describes the total force applied to the fluid per unit length [$\mathbf{f}(r,t)$] as a result of both the external force and the deformation of the boundary.

The system of differentio-integral equations given by Eqns 9–14 was solved on a rectangular grid with periodic boundary conditions in both directions, as described by Peskin and McQueen (1996). In this case, a skew symmetric operator was used to discretize the nonlinear term in the Navier–Stokes equations (Lai and Peskin, 2000). The velocity near the outer boundary of the domain was kept near zero on the edges of the domain by inserting four walls that were 30 spatial steps away from the edges of the fluid domain. The Navier–Stokes equations were discretized on a fixed Eulerian grid, and the immersed boundaries were discretized on a moving Lagrangian array of points. Unless otherwise stated, the fluid domain was 1230×1230 mesh widths in all simulations. At this mesh width, the two wings were separated by 10 mesh widths at their closest approach. The wings were each discretized into 120 spatial steps.

Lift and drag forces were calculated as functions of time by taking the opposite sign of the force applied to the fluid by one wing at each time step. By convention, lift and drag coefficients were calculated as follows:

$$C_L = \frac{2F_L}{\rho S U^2} \quad (15)$$

and

$$C_D = \frac{2F_D}{\rho S U^2}, \quad (16)$$

where C_L is the lift coefficient, C_D is the drag coefficient, F_D is the drag force per unit spanwise length, F_L is the lift

force per unit spanwise length, S is a characteristic area (chord length of the wing multiplied by unit length), U is the speed of the wing, and ρ is the density of the fluid. In these definitions, ‘spanwise’ refers to the direction perpendicular to the plane for two-dimensional simulations. Since these definitions are designed for the high Re case ($Re \gg 1$), C_D and C_L become functions of Re for intermediate values of Re .

Validation of the method

To test for the convergence of the numerical method, two simulations were considered: one at the mesh width used for all of the simulations presented in the Results and the other at half that mesh width. For the convergence test, the size of the fluid domain was reduced in both cases from $1 \text{ m} \times 1 \text{ m}$ to $0.5 \text{ m} \times 0.5 \text{ m}$ in order to make the fine grid computation practical. This pair of simulations modeled a two-winged fling half-stroke at $Re=128$. The particular wing kinematics used here are the same as those described in the case of a fling half-stroke. The resulting lift and drag coefficients are plotted as functions of dimensionless time in Fig. 3. In general, there is good agreement between the two mesh widths. Small deviations appear during rotational fling. This does not appear to introduce error for the rest of the stroke.

Comparison to experimental and numerical data for one-winged strokes

In order to check the method against recent experimental and numerical data, four sinusoidal one-winged flapping strokes similar to that of Wang et al. (2004) were modeled. The equations of motion of the wing are as follows:

$$x(t) = \frac{A_0}{2} \cos(2\pi f t) \quad (17)$$

and

$$\alpha(t) = \alpha_0 + \beta \sin(2\pi f t + \phi), \quad (18)$$

where A_0 is stroke amplitude, $x(t)$ describes the horizontal position of the center of the wing as a function of time, and $\alpha(t)$ describes the angle of attack relative to the x -axis as a function of time, ϕ sets the timing of rotation and β sets the change in angle of attack during stroke reversal. Basically, the wing flaps back and forth along a horizontal plane with a frequency of f . In this case, A_0/c was set to 2.8, ϕ was set to 0, and β was set to $\pi/2$. This provides a symmetric stroke with a minimum angle of attack of 45° . In order to obtain $Re=75$, f was set equal to $75\nu/\pi c A_0$. Lift and drag coefficients were normalized in the same manner as the two-dimensional elliptic wing described in Wang et al. (2004).

Lift and drag coefficients as functions of time for all cases are shown in Fig. 4. The green lines show the results of the immersed boundary simulation, the blue lines represent numerical data for a two-dimensional elliptic wing, and the red lines describe the experimental data for a three-dimensional model wing (Wang et al., 2004). There is

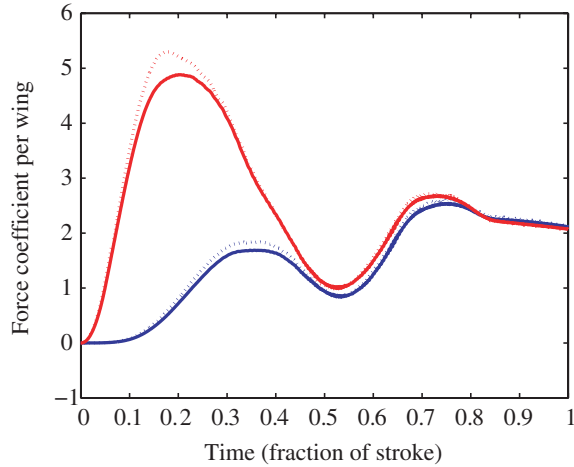


Fig. 3. Lift (blue) and drag (red) coefficients per wing during a two-winged fling half-stroke are plotted for two mesh widths. The coarser grid (dotted line) has a mesh width of about 8.33×10^{-4} m (the same mesh width as the other simulations in this paper), and the finer grid (solid line) has a mesh width of about 4.17×10^{-4} m. The two grid sizes show good agreement with small deviations occurring during the rotational part of fling.

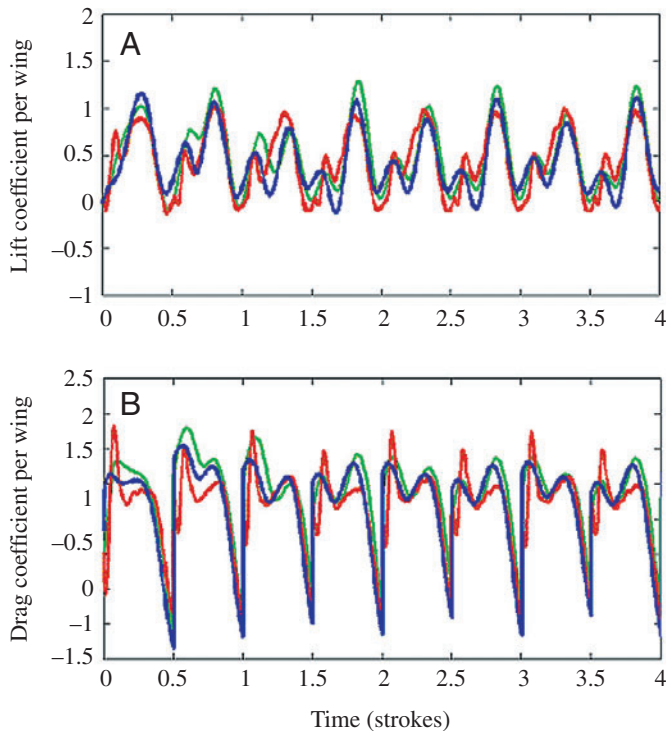


Fig. 4. Lift (A) and drag (B) coefficients for four sinusoidal strokes. The green lines show the results of the immersed boundary simulation, the blue lines represent numerical data for a two-dimensional elliptic wing (Wang et al., 2004), and the red lines describe the experimental data for a three-dimensional model wing (Wang et al., 2004). In all cases, the leading edge vortex did not appear to separate during translation. The wing in each case flaps in a sinusoidal motion with $\phi=0$, $\beta=\pi/2$, and $A_0/c=2.8$, as defined in Eqns 17 and 18, at $Re=75$. This represents a 2.8 chord translation and a minimum angle of attack of 45° .

excellent agreement between the two-dimensional immersed boundary simulation and the numerical simulation of a rigid elliptic wing given by Wang et al. (2004). In both simulations, the leading edge vortex did not appear to separate during wing translation, and lift coefficients agree well with the three-dimensional experiment. The small differences between our simulation and that of Wang et al. (2004) are probably due to a combination of differences in design (a flexible plate vs. a rigid ellipse) and numerical error. Differences between the simulations and the experiment are most likely due to differences in two and three dimensions as well as experimental and numerical error.

Comparison to experimental and numerical data for two-winged fling

In order to check the method for accuracy in describing wing-wing interactions, fling simulations similar to those described by experimentally by Spedding and Maxworthy (1986) and numerically by Sun and Yu (2003) were performed. At the beginning of the simulation, two wings were held

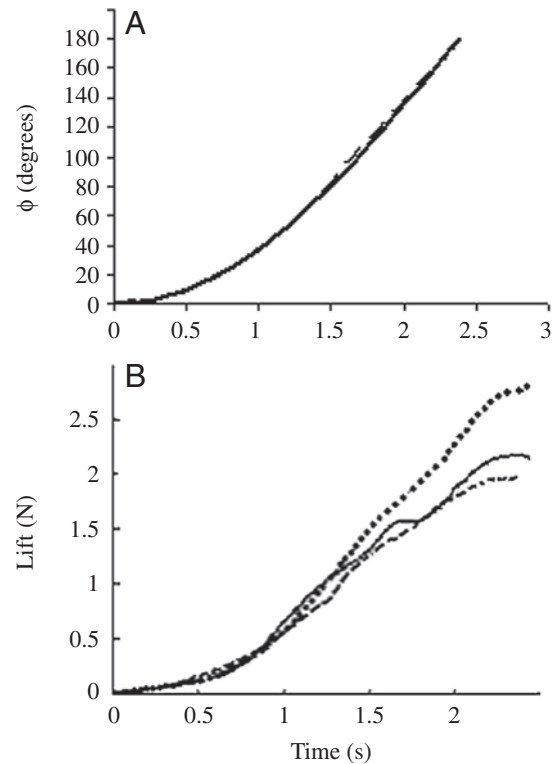


Fig. 5. Rotational motion $\Phi(t)$ of two wings during fling and the corresponding lift forces. (A) The broken line represents the motion used in the clap and fling experiments of Spedding and Maxworthy (1986). The solid line represents the rotational motion of the wings used in the immersed boundary simulation. The motion used by Sun and Yu (2003) is nearly identical. (B) The dotted line represents the lift forces measured over time in Spedding and Maxworthy's experiment at a Reynolds number (Re) of about 3×10^3 . The solid line represents the lift forces calculated by Sun and Yu at the same Re . The broken line represents the scaled lift forces calculated over time in the immersed boundary simulation at $Re=128$.

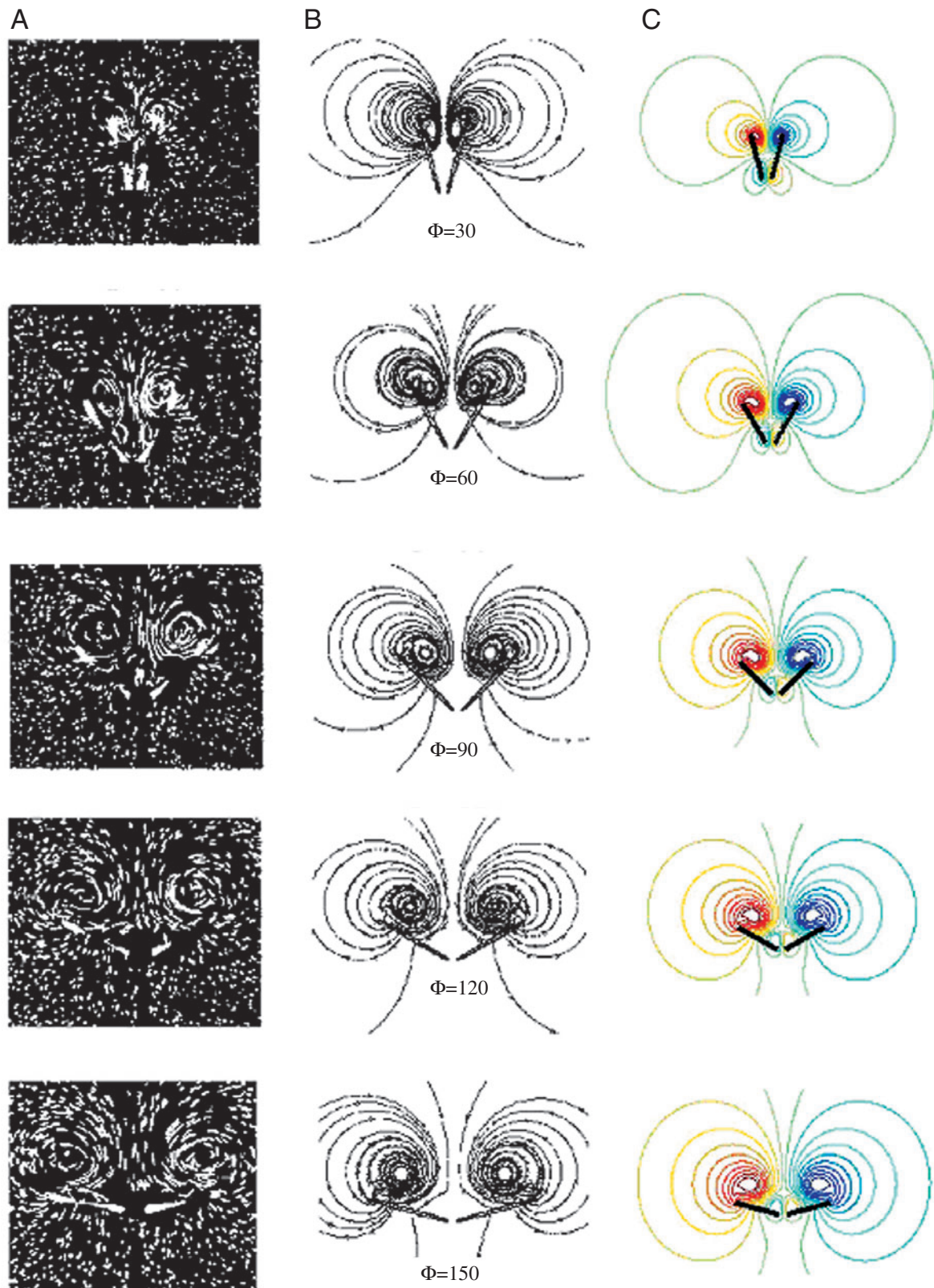


Fig. 6. Flow visualization and streamline plots of rotational fling at five points in time. The wing motion used in each case is shown in Fig. 5A. (A) Flow visualization of fling captured by Spedding and Maxworthy (1986) at a Reynolds number (Re) $\sim 3 \times 10^3$. (B) Streamline plots of fling calculated numerically for two rigid elliptic wings by Sun and Yu (2003) at $Re \sim 3 \times 10^3$. (C) Streamline plots of fling calculated from immersed boundary simulations at $Re \sim 128$. In all cases, two large leading vortices form and appear to remain attached to each wing during rotation.

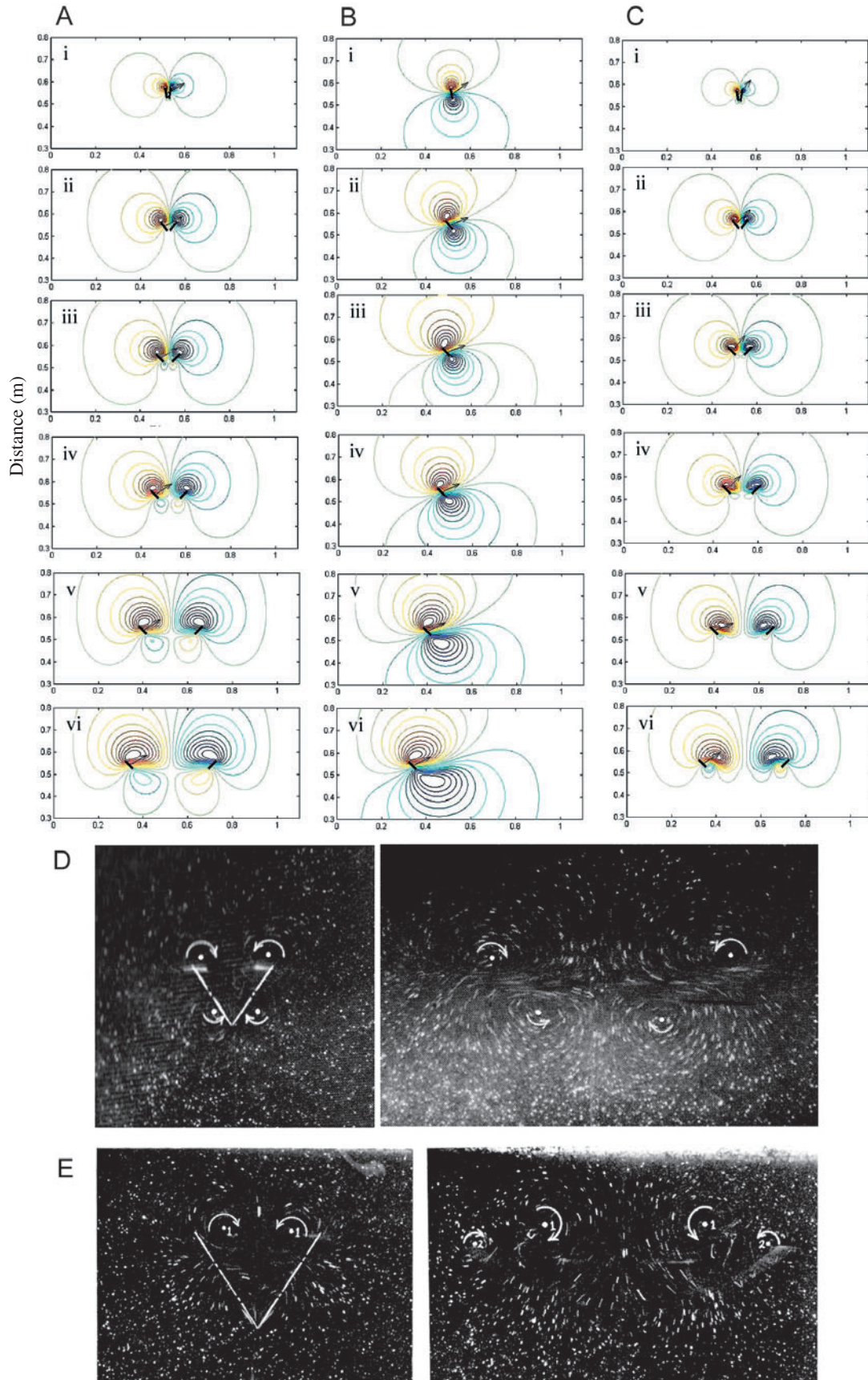


Fig. 7

parallel to each other at an angle of attack $\alpha=90^\circ$. The angle between the two wings, Φ , was initially set to 0° , and the distance between the wings was set equal to $0.10c$. The wings were then rotated apart along their trailing edge until $\Phi=180^\circ$. Spedding and Maxworthy measured lift forces during this simplified fling motion at $Re=3.0\times 10^3$. This Re is well above those considered in this paper ($8 < Re < 128$), and is beyond the range for which the immersed boundary method provides reasonable results. To make a comparison between the immersed boundary simulation and the experiment, the simulation was performed at $Re=128$. The forces were scaled up to $Re=3.0\times 10^3$ by calculating the lift coefficient as a function of time, and setting the scaled force equal to $F_{\text{scaled}}=1/2\rho C_D S \bar{U}_{\text{max}}^2$, where S is the surface area of the experimental wing (0.03 m^2), \bar{U}_{max} is the maximum velocity at the midpoint of the wing (0.018 m s^{-1}), and ρ is the density of the fluid (1030 kg m^{-3}). The numerical simulation of Sun and Yu was also performed at $Re=3.0\times 10^3$, using two elliptic wings with a thickness of $0.04c$ and placed $0.08c$ apart.

The exact wing motion used in this simulation and the experiment of Spedding and Maxworthy (1986) is shown in Fig. 5A. The wing motion used by Sun and Yu (2003) is nearly identical. The lift forces as functions of time for the immersed boundary simulation (broken line), the numerical simulation of Sun and Yu (solid line), and the physical experiment of Spedding and Maxworthy (dotted line) are shown in Fig. 5B. There is reasonable agreement between all three methods, and there is excellent agreement between the two-dimensional

numerical simulations. Flow visualization and the corresponding streamline plots of the numerical simulations are shown at five stages during fling in Fig. 6. In all cases, two large leading edge vortices form and appear to remain attached to each wing during rotation. A second pair of small vortices also forms along the trailing edge.

Results

Fling

In order to determine the effect of Re on the lift generated during fling, simulations using either one wing or two wings following the motion described in Materials and methods were performed for Re ranging from 8 to 128. The Re was varied by changing the velocity of the wing and holding all other parameters constant.

The streamlines of the flow around two wings and one wing at $Re=8$ and two wings at $Re=128$ performing the same fling motion are shown at six selected times in Fig. 7. The streamlines are curves which have the same direction at each point in the fluid as the instantaneous fluid velocity $\mathbf{u}(\mathbf{x},t)$. The density of the streamlines in each plot is proportional to the speed of the flow. For more details on how the plots were generated see Miller and Peskin (2004). Normalized force vectors at each point in time were also drawn on the wing to display the direction of the force that the fluid applies to the wing.

In the two-winged case with $Re=8$ (Fig. 7A), the streamlines of the flow during wing rotation are qualitatively similar to those described by Lighthill (1973), calculated numerically by Haussling (1979), and observed experimentally by Maxworthy (1979), as shown in Fig. 7D. As the wings rotate apart along the trailing edge, two large leading edge vortices are formed on each wing (Fig. 7Ai–iii). No trailing edge vortices are formed until the wings begin to translate apart. At the beginning of translation, two weak trailing edge vortices begin to form on each wing (Fig. 7Aiii–iv). As the wings continue to translate away from each other, the attached trailing edge vortices grow in strength (Fig. 7Aiv–vi). The strengths of the trailing edge vortices, however, are *much* less than the strengths of the leading edge vortices throughout the *entire* stroke considered here. Fig. 7D shows flow visualization of fling and subsequent translation at Re about 32 given by Maxworthy (1979). Similar to the numerical results, two large leading edge vortices form during rotation, and two smaller trailing edge vortices form and grow during translation. Both sets of leading and trailing edge vortices do not appear to separate from the wing. The streamline plots at $Re=16$ and $Re=32$ are similar to those described here.

In the one-winged case with $Re=8$, both a leading and a trailing edge vortex are formed at the beginning of rotation (Fig. 7Bi–iii). This phenomenon is consistent with the principle of total vorticity conservation. Consider an infinite fluid domain with a finite number of immersed solids that are a finite distance apart. If the fluid and solid bodies are initially at rest, then the total vorticity in the system (including the solid

Fig. 7. Streamlines of the fluid flow around two wings (A) and one wing (B) at a Reynolds number of 8 and around two wings (C) at a Reynolds number (Re) of 128 for a fling half-stroke. The arrow on the left wing shows the direction of the normalized force acting on the wing at each time (i–vi). The wings begin at an angle of attack of 90° and rotate about the trailing edge to an angle of attack of 45° . (A) During rotation, attached leading edge vortices are formed on each wing and no trailing edge vortices are formed (i–iii). When translation begins, small attached trailing edge vortices begin to form (iii–v). As the trailing edge vortices grow in size relative to the leading edge vortices, lift is reduced. The leading edge vortices, however, remain larger than the trailing edge vortices for most of the half-stroke (v–vi). (B) In the one wing case, attached leading edge and trailing edge vortices are formed during rotation (i–iii). When translation begins, equally sized leading and trailing edge vortices are attached to the wing, creating substantially lower lift forces in comparison to the two-winged case (iii–vi). (C) At a Reynolds number (Re) of 128, attached leading edge vortices are formed on each wing and no trailing edge vortices are formed initially (i–iii). When translation begins, however, the leading edge vortices are shed, and trailing edge vortices are formed (v–vi). The trailing edge vortex grows in size and is subsequently shed from the wing as a new leading edge vortex begins to form. (D) Flow visualization of fling at $Re=30$ by Maxworthy (1979). Similar to case A, a pair of large leading edge vortices is formed and remains attached to the wing during rotation. A smaller pair of trailing edge vortices is formed and grows during translation. (E) Flow visualization of fling at $Re=1.3\times 10^4$. Similar to case C, a pair of large leading edge vortices (1) forms during rotation and is shed during translation. A new pair of leading edge vortices forms during translation (2).

bodies) must remain zero for all time. In this case, the leading and trailing edge vortices spin in opposite directions during rotation and translation. Since the wings are infinitely thin, we can consider vorticity only within the fluid domain, and the principle of vorticity conservation demands that leading and trailing edge vortices cancel so that the total vorticity in the system is zero. This implies that the leading and trailing edge vortices are of equal and opposite strength. During translation, these two vortices remain attached to the wing until wing reversal (Fig. 7Biv–vi). This situation is markedly different from the two-winged case: leading and trailing edge vortices are formed during rotation in the one-winged case, while two leading edge vortices and no trailing edge vortices are formed in the two-winged case. During translation, leading and trailing edge vortices of equal strength are attached to the wing in the one-winged case, while a strong leading edge vortex and a weak trailing edge vortex form and remain attached to each wing in the two-winged case.

At $Re=128$ (Fig. 7C), the aerodynamics during the two-winged fling differ from the corresponding cases at $Re=32$ and below. At the beginning of the half-stroke, two strong leading edge vortices are formed during wing rotation (Fig. 7Ci–ii). As the wings translate apart, weak trailing edge vortices are formed and begin to grow (Fig. 7Ciii–iv). Unlike the low Re case, the leading edge vortices are shed at the beginning of translation (Fig. 7Civ–v). During translation, a second pair of leading edge vortices are formed and begin to grow. This same phenomenon was observed by Maxworthy (1979) at higher Re

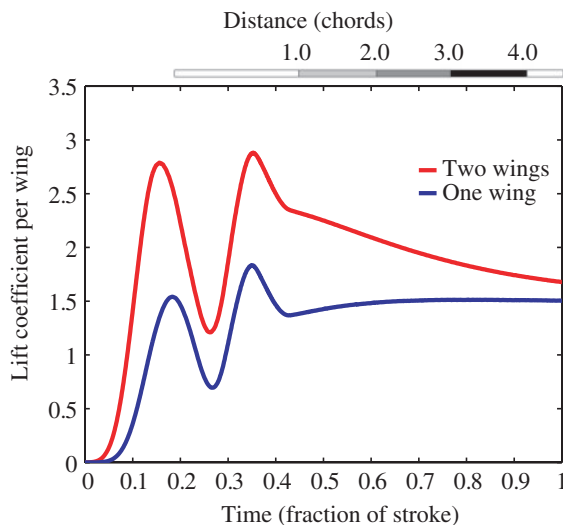


Fig. 8. Lift coefficients per wing at a Reynolds number of 8 are plotted as functions of time for the fling half-strokes shown in Fig. 7A,B. The bar at the top of the graph shows the number of chord lengths traveled. The first peak in the lift coefficients corresponds to the large lift forces generated during wing rotation. The second peak in the lift coefficients corresponds to the period of translational acceleration. The lift forces per wing are on average about 35% greater during translation after clap and fling than during the steady translation of a single wing with no clap and fling (this average was taken over the fraction of the stroke from 0.37 to 1, after rotation had finished).

(Fig. 7E). Two large leading edge vortices (1) are formed during rotation. As translation begins, the pair of rotational leading edge vortices is shed, and a second pair of leading edge vortices (2) is formed. In the immersed boundary simulation, the trailing edge vortices are shed as translation continues (Fig. 7Cv–vi). The alternate vortex shedding at higher Re corresponds to the formation of the von Karman vortex street. It is important, however, to note that in three-dimensional insect flight at higher Re , alternate vortex shedding does not occur (Birch et al., 2004). Instead, the leading edge vortex remains attached to the wing until wing reversal and the trailing edge vortex is initially shed. Presumably, the leading edge vortex would remain attached to the wing during three-dimensional clap and fling at higher Re , generating larger lift coefficients for both the two- and one-winged cases.

The lift coefficients as functions of dimensionless time (fraction of stroke) for the one- and two-winged cases at $Re=8$ are plotted in Fig. 8. The bar at the top of the graph shows the number of chord lengths traveled. The first peak in the lift coefficients corresponds to the large lift forces generated during wing rotation. The second peak in the lift coefficients corresponds to the period of translational acceleration. The average lift per wing generated during wing rotation in the two-winged case is about twice that generated in the one-winged

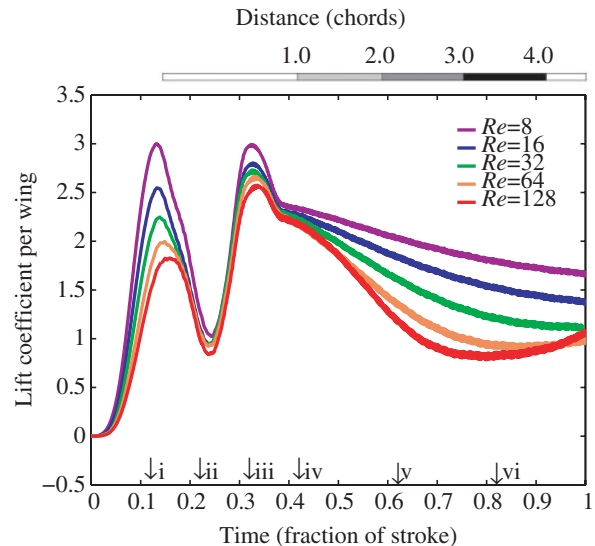


Fig. 9. Lift coefficients are plotted as functions of time for a two-winged clap and fling half-stroke. The bar at the top of the graph shows the number of chord lengths traveled. The letters i–vi along the x axis correspond to the times the streamlined plots labelled i–vi in Fig. 7A,C were drawn. The angles of attack during pure translation were set to 45° . Reynolds number (Re) was varied by changing the translational velocity of the wing from 0.00375 to 0.06 m s^{-1} . The first peak corresponds to the lift generated during wing rotation, and the second peak corresponds to the lift generated during translational acceleration. The lift enhancing mechanisms of fling decrease with increasing Re . For $Re=32$ and below, lift coefficients decrease during translation after fling as the trailing edge vortex grows in strength. For $Re=64$ and above, lift coefficients fall as the leading edge vortices separate from the wings.

case. In addition, the lift forces are about 70% greater in the two-winged case than in the one-winged case at the beginning of constant translation. Lift forces per wing in the two-winged case are on average about 35% higher than in the one-wing case during the entire 4.5 chord length translation. Another interesting phenomenon seen in the one-winged case is that lift is slow to develop over the first couple chord lengths of translation. This is most likely due to the Wagner effect, in which the proximity of the trailing edge vortex to the wing transiently reduces the lift until it moves sufficiently downstream of the wing. This idea is supported by the fact that the phenomenon is not observed in the two-winged case where the trailing edge vortices are initially absent. Both one- and two-winged lift forces approach the same steady lift values at the end of translation. These force traces are very similar to those calculated by Sun and Yu (2003) at $Re=17$ using a similar two-winged fling motion. The wings in their simulation were 0.08 chord lengths apart at the beginning of the stroke rotated at a faster angular velocity. The average lift coefficient over the entire 3-chord-length half stroke (rotation and translation) in their simulation was 2.4 for two wings and 1.0 for one wing.

Lift coefficients for a range of Re are plotted as functions of dimensionless time for two-winged fling in Fig. 9. The first peak corresponds to the lift generated during wing rotation, and the second peak corresponds to the lift generated during translational acceleration. For $Re=32$ and below, the different cases are similar. Lift coefficients decrease during translation

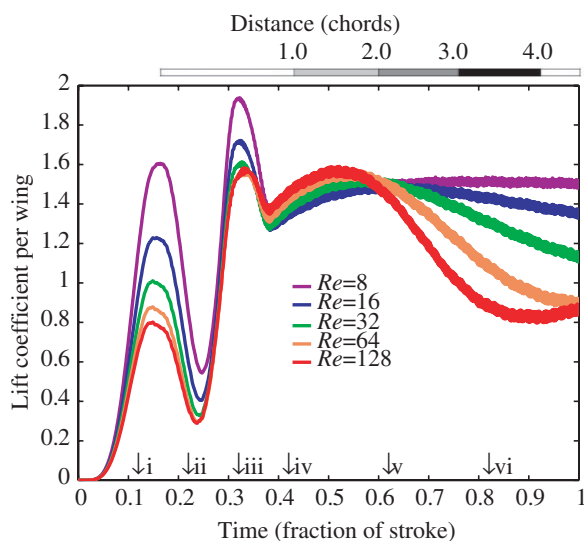


Fig. 10. Lift coefficients are plotted as functions of time for a one-winged fling half-stroke. The letters i–vi along the x axis correspond to the times the streamlined plots labelled i–vi in Fig. 7B were drawn. The angle of attack during pure translation was set to 45° . The Reynolds number (Re) was varied by changing the translational velocity of the wing from 0.00375 to 0.06 m s^{-1} . The first peak in lift corresponds to the lift forces generated during wing rotation. The second peak corresponds to the lift forces generated during translational acceleration. For $Re=64$ and above, lift coefficients fall as the leading edge vortices separate from the wings.

as the trailing edge vortex grows. Lift is also enhanced for longer periods of time at lower Re (the relative difference in strength between the attached leading and trailing edge vortices persists longer for lower Re). The growth of the trailing edge vortex during translation and resulting drop in lift was also observed by Sun and Yu (2003) at a $Re=17$. For $Re=64$ and higher, the leading edge vortex is shed at the beginning of translation, and lift forces subsequently drop. Lift forces grow again as a new leading edge vortex is formed and the trailing edge vortex is shed. This may not be obvious in Fig. 9, but the growth in lift followed by force oscillations become apparent when longer periods of time are plotted. As stated earlier, the three-dimensional case of flight at higher Re does not involve oscillating lift forces since alternate vortex shedding does not occur. It is also important to note that the leading edge vortex is shed after about 1 chord length of travel. Other studies, including a two-dimensional experiment (Dickinson and Götz, 1993) and a two-dimensional numerical simulation (Wang et al., 2004), show that the separation of the leading edge vortex and subsequent lift drop does not occur until about 2.5–3.5 chord lengths of travel. Flow visualization by Maxworthy (1979), as well as these simulations, show that the leading edge vortex is shed near the beginning of translation after fling at higher Re . This suggests that the separation of the leading edge vortex from the wing could depend upon wing-wing interactions and the kinematics of rotation.

Lift coefficients for a range of Re are plotted as functions of dimensionless time for one-winged fling in Fig. 10. The first

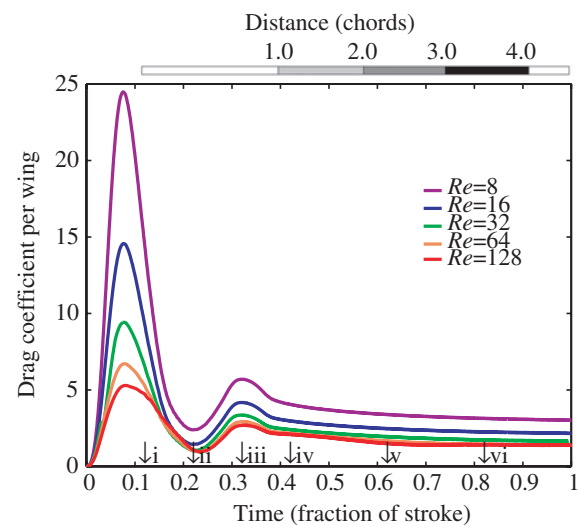


Fig. 11. Drag coefficients are plotted as functions of time for a two-winged fling half-stroke. The letters i–vi along the x axis correspond to the times the streamlined plots labelled i–vi in Fig. 7A,C were drawn. The angles of attack during pure translation were set to 45° . Reynolds number (Re) was varied by changing the translational velocity of the wing from 0.00375 to 0.06 m s^{-1} . The first large peak corresponds to drag generated during wing rotation. The second smaller peak corresponds to drag forces generated during translational acceleration. Drag coefficients increase with decreasing Re . This inverse relationship is particularly significant during the initial wing rotation.

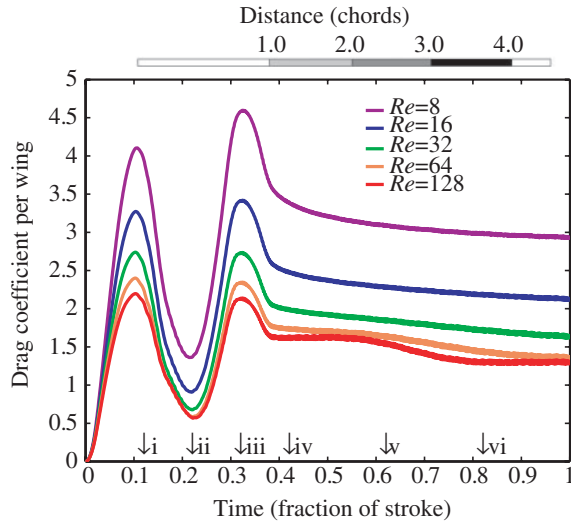


Fig. 12. Drag coefficients plotted as functions of time for a one-winged fling half-stroke. The letters i–vi along the x axis correspond to the times the streamlined plots labelled i–vi in Fig. 7B were drawn. The angles of attack during pure translation were set to 45° . Reynolds number (Re) was varied by changing the translational velocity of the wing from 0.00375 to 0.06 m s^{-1} . The first peak corresponds to the drag forces generated during translational acceleration. Note that the drag forces per wing generated during rotation in the one-winged case are significantly smaller than those generated per wing in the two-winged case (see Fig. 11). In general, drag coefficients increase with decreasing Re .

peak corresponds to the lift forces produced during wing rotation, and the second peak corresponds to the lift forces generated during translational acceleration. Lift coefficients for periods of rotation and acceleration are higher at lower Re . This phenomenon might be due to the larger effect of added mass at lower Re . As the Re decreases, the width of the boundary layer around the wing grows, and the mass of the fluid ‘entrained’ by the wing is larger. Lift coefficients are also substantially lower at all times and for all Re considered when compared to the respective two-winged cases (note the difference in scales between Figs 9 and 10). For $Re=64$ and higher, lift begins to drop after about 2.5 chord lengths of travel during translation due to the separation of the leading edge vortex. Presumably, translational lift forces would be higher in three-dimensional flight since the leading edge vortices would not be shed.

Drag coefficients for a range of Re are plotted as functions of dimensionless time for two-winged fling in Fig. 11. The first peak in each of the drag coefficient plots corresponds to the large drag forces produced as the two wings are rotated apart. The maximum drag coefficient produced during rotation increases significantly as the Re is decreased. The smaller second peak in drag coefficients corresponds to the forces generated during the translational acceleration of the wings at the beginning of the half-stroke. This translational drag coefficient also increases with decreasing Re , but the effect is substantially smaller than that produced during wing rotation.

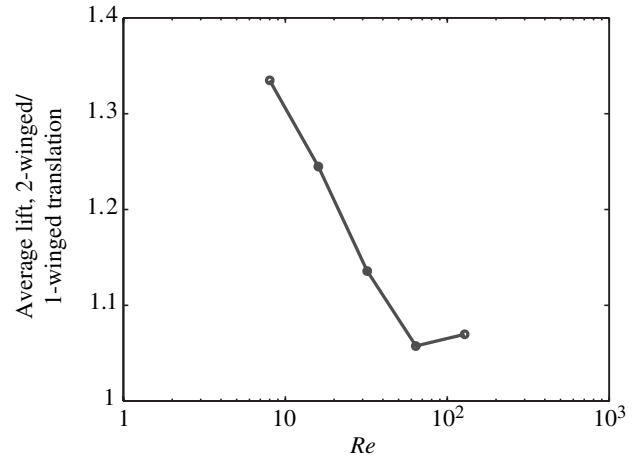


Fig. 13. The average lift coefficients per wing during translation following two-winged fling divided by the corresponding average lift coefficients for one-winged fling vs Reynolds number (Re). The average lift coefficients following fling were calculated as the average lift coefficients generated after rotation and translational acceleration and during translation at a constant angle of attack. This value decreases with increasing Re , suggesting that the lift enhancing effects of clap and fling are more significant at lower Re .

Drag coefficients for all Re gradually decrease during translation to steady values.

Drag coefficients for a range of Re are plotted as functions of dimensionless time for one-winged fling in Fig. 12. The first peak in the drag coefficients corresponds to the drag forces produced during the rotation of a single wing. These drag forces are significantly smaller than those produced during rotation with two wings (note the difference in scales between Figs 11 and 12). The second peak in the drag coefficient corresponds to the drag forces produced during the translational acceleration of the wing. After acceleration, the

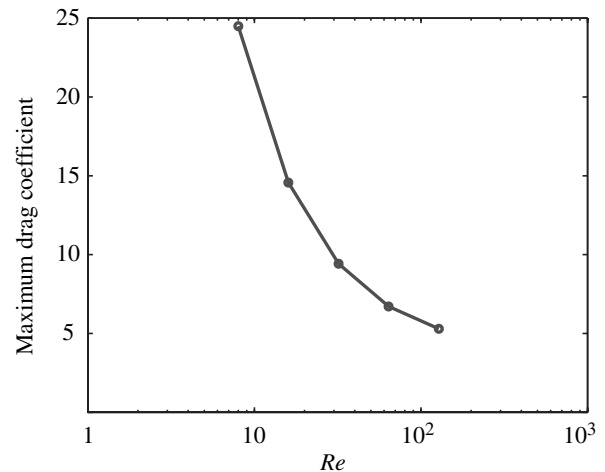


Fig. 14. The maximum drag coefficient during the rotation of the wings at the beginning of fling plotted against the Reynolds number (Re). The drag coefficient significantly increases for decreasing Re . This result suggests that relatively larger forces are needed for tiny insects to rotate their wings and perform a ‘fling’.

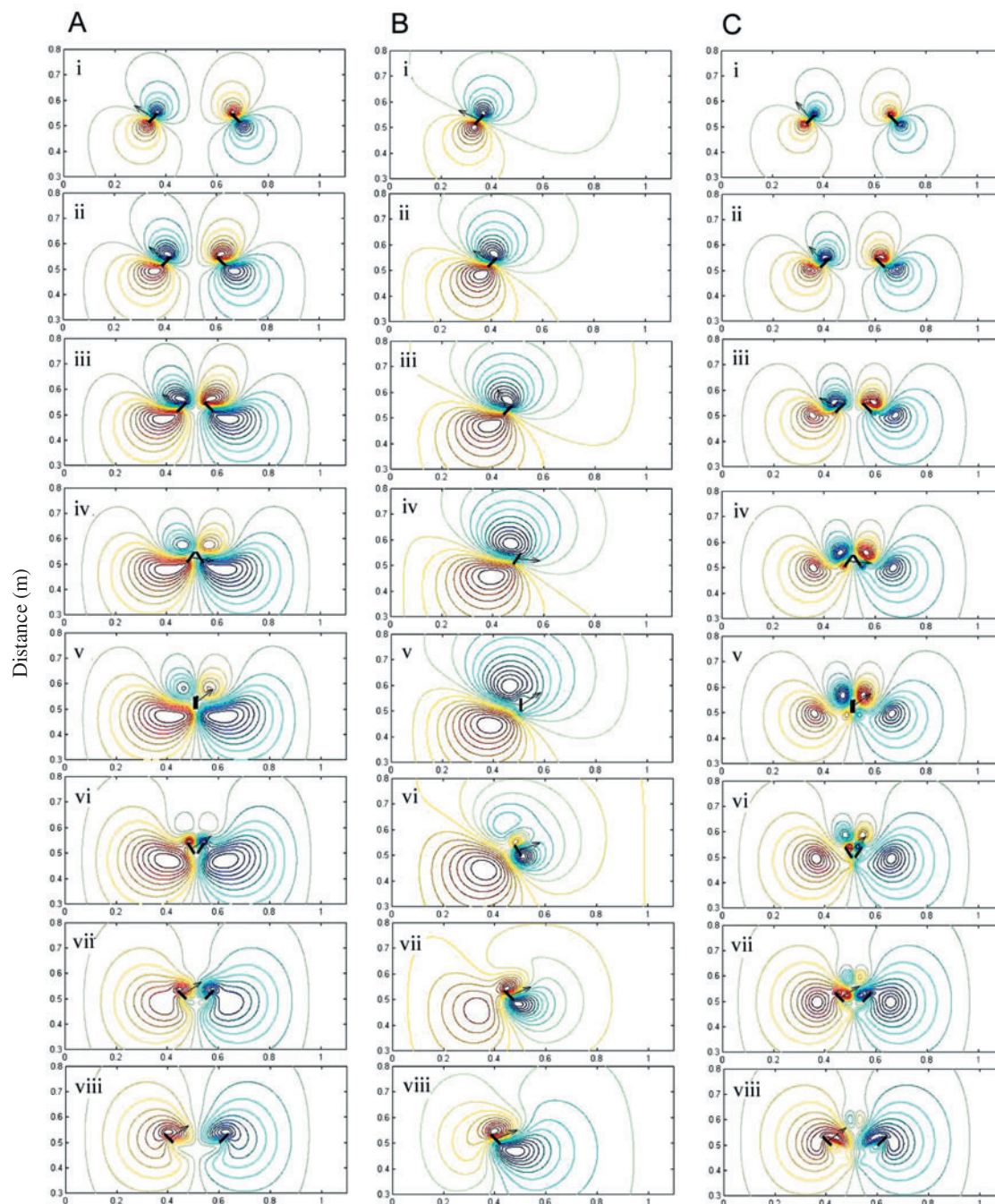


Fig. 15. Streamlines of fluid flow around two wings (A) and around one wing (B) during a full clap and fling stroke at a Reynolds number (Re) of 8 and around two wings at $Re=128$ (C). The arrow on the left wing shows the direction of the normalized force acting on the wing. (A) During translation, leading and trailing edge vortices form and remain attached to the wing (i–iii). During ‘clap’, the wings rotate together at the end of translation (iv–v). At this time, the leading and trailing edge vortices are shed. During ‘fling’, the wings rotate apart forming two new leading edge vortices (vi). Towards the end of rotation, the wings are translated apart at a constant angle of attack and speed (vi–viii). During translation, the leading edge vortices remain attached to the wing, and weak trailing edge vortices are formed. (B) Large leading and trailing edge vortices are formed during the initial translation of the wing (i–iii). This pair of vortices is shed during rotation (iv–v), and a new pair of leading and trailing edge vortices is formed during the subsequent translation (vi–viii). Note that in the two winged case, no trailing edge vortices are formed during wing rotation, and much smaller trailing edge vortices are formed during the subsequent translation. (C) At $Re=128$, leading edge vortices are formed and the trailing edge vortices are shed (i–iii). After a translation of about 2.5 chord lengths, the leading edge vortices begin to separate from the wings (iii). During ‘clap’, the wings rotate together at the end of translation (iv–v). At this time, the leading and trailing edge vortices are shed. During ‘fling’, the wings rotate apart. Two large leading edge vortices are formed, and no trailing edge vortices are formed initially (v–vi). Towards the end of rotation, the wings are translated away from each other and the pair of leading edge vortices formed during rotation is shed. A second pair of leading edge vortices begins to form near the end of translation (vi–viii).

drag coefficients gradually decrease to steady values. Similar to the two-winged case, drag coefficients during one-winged fling increase with decreasing Re .

The average lift per wing generated during translation after a two-winged fling half-stroke divided by the average lift per wing generated during translation after a one-winged fling half-stroke are plotted for a range of Re in Fig. 13. The average lift coefficients per wing were calculated as the average lift after translational acceleration and during the steady translation of the wing at a constant angle of attack (0.37–1.0 fraction of the half stroke). For $Re=8$, the average lift generated during a 4.5 chord translation after two-winged fling is on average 35% larger than the average lift generated during translation after one-winged fling. Lift enhancement provided by two-winged fling decreases with increasing Re . For a $Re=128$, the average lift per wing produced during translation after two-winged fling is about equal to the average lift generated during translation following a one-winged fling. It is important to note that these ratios only consider the effect of lift enhancement after rotation and acceleration.

The maximum drag coefficients produced during rotation for two-winged fling for a range of Re are plotted in Fig. 14. The drag coefficients produced during rotational fling sharply increase with decreasing Re . This same phenomenon is also true during all periods of rotation and acceleration. The Re effect is, however, most pronounced during fling. This relationship suggests that tiny insects must apply large forces to the fluid to turn and rotate their wings. Perhaps flexible wings and setal fringing reduce this Re effect.

Clap and fling

The streamlines of the flow around two wings and one wing performing a complete clap and fling stroke at a $Re=8$ are shown at eight points in time in Fig. 15A,B. In each case, the wings accelerate from rest and move towards each other at a constant translational speed. At a $Re=8$, leading and trailing edge vortices form and remain attached to each of the wings during the first half-stroke (Fig. 15Ai–iii). As the wings near each other, they begin to rotate and ‘clap’ together (Fig. 15Aiv–v). During this rotation, the leading and trailing edge vortices are shed. The wings then rotate apart and translate away from each other during ‘fling’ (Fig. 15Avi–viii). This is similar to the previous case of simple ‘fling’, except that the wings are now translating through their wakes. During rotation (Fig. 15Avi), new leading edge vortices are formed on each wing, and no trailing edge vortices are formed initially. As the wings translate away from each other, they move back through their wakes, and weak trailing edge vortices are formed (Fig. 15Avii–viii). In the case of one wing, a pair of leading and trailing edge vortices is formed during the initial translation (Fig. 15Bi–iii). These vortices are then shed during wing rotation (Fig. 15Biv–v). During the downstroke, a pair of large leading and trailing edge vortices is formed. This is different from the two-winged case where only two large leading edge vortices are formed initially.

The streamlines of the flow around two wings performing a

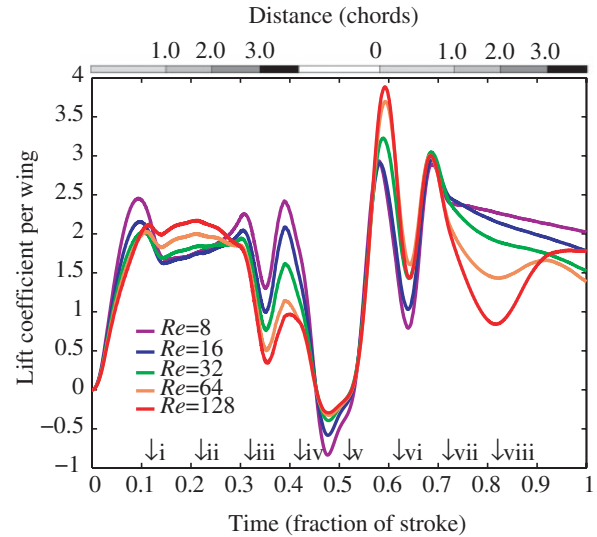


Fig. 16. Lift coefficients as functions of time for a two-winged clap and fling stroke. The letters i–viii along the x axis correspond to the times the streamlined plots labelled i–viii in Fig. 15A,C were drawn. The angle of attack during pure translation was set to 45° . The Reynolds number (Re) was varied by changing the translational velocity of the wing from 0.00375 to 0.06 m s^{-1} . In general, lift coefficients were larger at higher Re during the initial upstroke. Lift coefficients, however, were smaller at higher Re during fling and subsequent translation. For $Re=64$ and higher, lift coefficients peak during translational acceleration and rotation. Lift coefficients drop when the leading edge vortices separate from the wings (vii–viii). For $Re=32$ and below, lift coefficients also peak during translational acceleration and rotation. Lift coefficients are relatively constant during translation in the first half-stroke (i–iii). Lift coefficients are transiently augmented during translation after fling (vi–viii).

complete clap and fling stroke at a $Re=128$ are shown in Fig. 15C. The leading edge vortices are formed and the trailing edge vortices are shed during the initial translation of the wing (Fig. 15Ci–ii). The leading edge vortices begin to separate from the wing after a translation of about 2.5 chord lengths (Fig. 15Ciii). Lift drops as the wings near each other and clap together (Fig. 15Civ–v). During this rotation of the wings, the vortices from the first half-stroke are shed. The wings continue to rotate apart and then translate away from each other during ‘fling’ (Fig. 15Cv–vi). Similar to the previous case of a fling half-stroke, two large leading edge vortices are formed during rotation, and no trailing edge vortices are formed initially (Fig. 15Cvi). As the wings translate away from each other, the leading edge vortices are shed (Fig. 15Cvii), and new trailing edge vortices form and grow in strength. Later in the stroke, a second pair of leading edge vortices forms and grows in strength (Fig. 15Cviii).

Lift coefficients for a range of Re are plotted as functions of dimensionless time for two-winged clap and fling in Fig. 16. The markers on the time axis denote the points in time that the streamline plots in Fig. 15A,C were drawn. The lift coefficients naturally divide into two patterns, lift coefficients for $Re=64$ and above and lift coefficients for $Re=32$ and below.

The lift coefficients for $Re=32$ and below are characterized by relatively constant forces during translation due to the attachment of the leading and trailing edge vortices. The first peak in the lift coefficient corresponds to the forces produced during wing acceleration at the beginning of the stroke (i). During constant translation, lift coefficients initially drop and then gradually increase as the wings approach each other (ii–iii). Lift rapidly drops as the wings begin to decelerate (iii). When wing rotation begins, lift forces increase again as the wings clap together (iii–iv). Lift finally drops to about zero at the end of rotation (v). At the beginning of the second half-stroke (fling), lift coefficients peak as two large leading edge vortices are formed (v–vi). The next peak in lift (vi–vii) corresponds to the lift generated during translational acceleration. These translational lift coefficients are larger than those produced during the first half stroke. This lift enhancing effect is due to the asymmetry in the vortical field produced by the clap and fling motion.

The lift coefficients for $Re=64$ and above are characterized by unsteady lift forces due to vortex shedding. The initial peak in lift coefficients corresponds to the lift forces produced during the translational acceleration of the wings (i). During constant translation, the leading edge vortex begins to separate but lift does not drop significantly until a translation of about three chord lengths (ii–iii). Lift then drops as the two wings decelerate at the end of the upstroke and clap together (iv–v). At the beginning of the second half-stroke, lift is enhanced

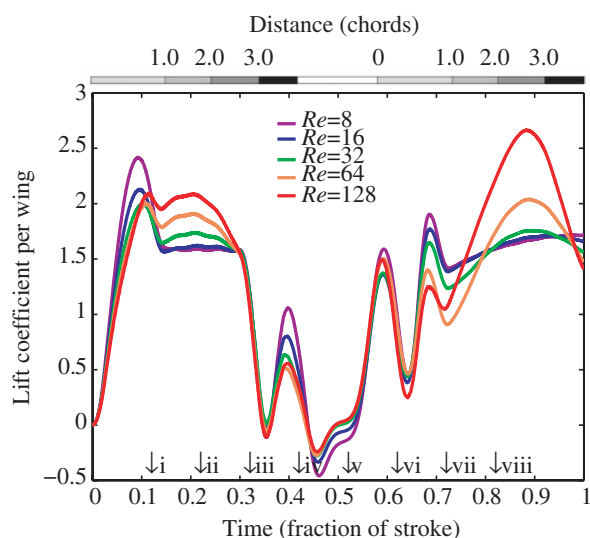


Fig. 17. Lift coefficients as functions of time for one wing moving with the same clap and fling motion as shown in Fig. 16. The letters i–viii along the x axis correspond to the times the streamlined plots labelled i–viii in Fig. 15B were drawn. The angle of attack during pure translation was set to 45° . The Reynolds number (Re) was varied by changing the translational velocity of the wing from 0.00375 to 0.06 m s^{-1} . In general, lift coefficients increase with Re . The lift forces generated during the initial upstroke are very similar to those shown in the two-winged case (i–iii). During fling, lift coefficients during rotation and the subsequent translation (vi–viii) are significantly less than the two-winged case for $Re=32$ and below.

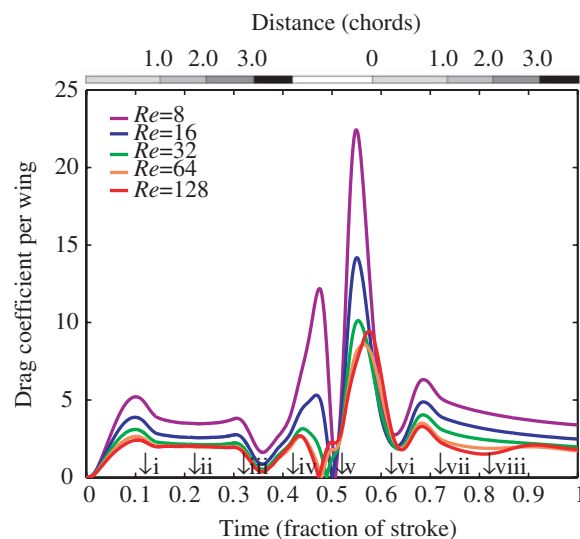


Fig. 18. Drag coefficients as functions of time for a two-winged clap and fling stroke. The letters i–viii along the x axis correspond to the times the streamlined plots labelled i–viii in Fig. 15A,C were drawn. The angle of attack during pure translation was set to 45° . The Reynolds number (Re) was varied by changing the translational velocity of the wing from 0.00375 to 0.06 m s^{-1} . In general, drag coefficients are larger for lower Re . This inverse relationship is most significant during periods of wing rotation (iv–vi). In general, drag forces peak during periods of acceleration and rotation and remain relatively constant during periods of pure translation.

when two large leading edge vortices are formed during rotation (v). As the wings begin to translate away from each other, the leading edge vortices are shed and trailing edge vortices grow (vi). Later during translation, the trailing edge vortices begin to separate from the wing, a new pair of leading edge vortices begins to grow, and the lift coefficient subsequently increases. This is consistent with the pattern of vortex shedding and growth visualized by Maxworthy (1979) at high Re . In Maxworthy's flow visualization, the initial pair of leading edge vortices is shed when translation begins, and a second pair of leading edge vortices begins to grow during translation.

Lift coefficients for one wing moving in a clap and fling motion are shown in Fig. 17 for a range of Re . The initial peak in lift corresponds to the lift forces generated during wing acceleration from rest. During upstroke translation, lift coefficients generally increase with increasing Re . For higher Re , the lift forces grow during the first three chord lengths of translation (ii–iii). The leading edge vortex then begins to separate from the wing, and the lift forces drop as the wing decelerates and begins to rotate (iv–v). During wing rotation, lift coefficients are slightly higher at lower Re . During translation, lift coefficients are higher at higher Re . For $Re=64$ and above, lift drops after a translation of about 2.5 chord lengths as the leading edge vortex separates from the wing. Dickinson (1994) measured lift forces experimentally on a wing moving with a two-dimensional motion similar to the motion used in this simulation. The lift coefficients

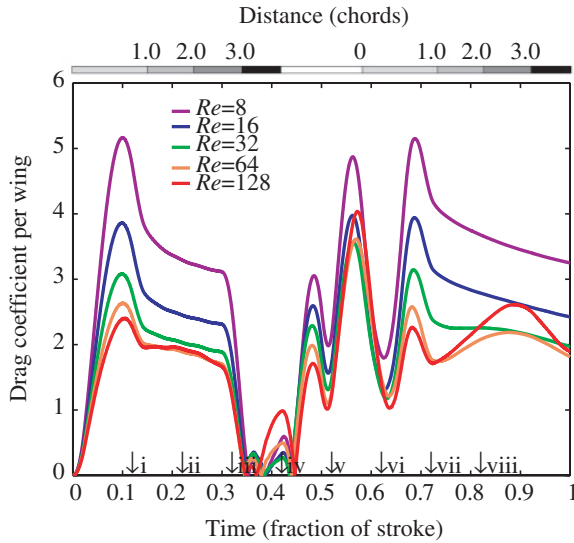


Fig. 19. Drag coefficients for one-winged fling as functions of time for a range of Reynolds numbers (Re). The letters i–viii along the x axis correspond to the times the streamlined plots labelled i–viii in Fig. 15B were drawn. The angle of attack during pure translation was set to 45° . In general, drag coefficients are smaller for higher Re . In comparison to the two-winged case, drag coefficients are significantly lower during ‘clap’ (the end of the upstroke) for all Re . During wing rotation at the beginning of the downstroke, drag coefficients are substantially lower than the two-winged case for all Re . The difference between the one and two-winged case is greatest at lower Re .

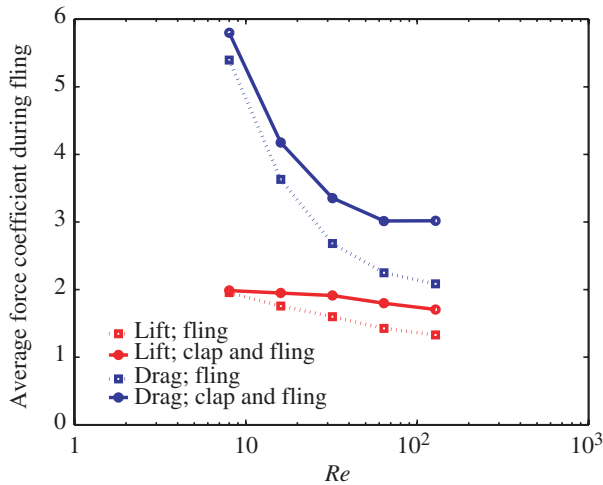


Fig. 20. The average lift and drag coefficients generated during fling for an entire fling half-stroke following a clap half-stroke and for an entire fling half-stroke started from rest as a function of the Reynolds number (Re). Force coefficients were averaged during wing rotation and a subsequent translation of about 3.5 chord lengths. Average lift coefficients increase slightly with decreasing Re . Average drag coefficients increase significantly as the Re is lowered. Force coefficients are higher for fling half-strokes that follow clap half-strokes as the wings move back through their wakes. This ‘wake capture’ effect decreases with decreasing Re .

measured over time in each case are remarkably similar. Lift forces peak during rotation and acceleration, fall to values near 1.5 during the first 2–2.5 chord lengths of translation, and drop to values near 1 as the leading edge vortex separates from the wing.

Drag coefficients for a range of Re are plotted as functions of dimensionless time for two-winged clap and fling in Fig. 18. The letter markers (i–vi) on the time axis denote the points in time when the streamline plots in Fig. 15A,C were drawn. In general, drag coefficients increase with decreasing Re . The first peak in the drag coefficients corresponds to the drag forces generated during the translational acceleration of the wing (i). Drag coefficients remain relatively constant during the translational phase of the first half-stroke (i–iii). The drag coefficients drop during wing deceleration, but sharply increase again when the wings are rotated (clapped) together (iv). At the beginning of the second half-stroke, the drag coefficients peak again as the wings are rotated apart (v–vi). There is a smaller peak during translational acceleration (vi–vii). Finally, the drag coefficients approach steady values as the wings translate apart (vii–viii). The Re differences in drag coefficients are most pronounced during wing rotation.

Drag coefficients for a range of Re during one-winged clap and fling are shown in Fig. 19. In general, drag coefficients are larger at lower Re throughout the entire stroke. In comparison to the two-winged case, drag coefficients per wing are lower throughout the stroke for the one-winged case at all Re . The differences between the one and two-winged cases are greatest during wing rotation (particularly during fling) and acceleration at lower Re . The drag coefficients over time in these simulations are also strikingly similar to those measured experimentally by Dickinson (1994) using one wing moving in a two-dimensional motion.

Fig. 20 shows the average lift and drag coefficients generated during a fling half-stroke started from rest and a fling half-stroke

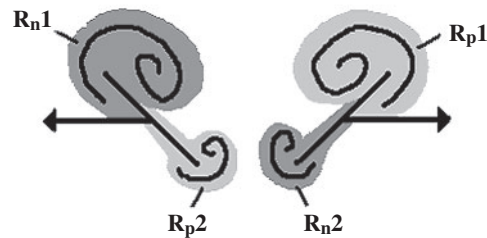


Fig. 21. Regions of positive and negative vorticity during the translation of two wings following ‘clap and fling’. R_{n1} and R_{n2} denote regions of negative vorticity, R_{p1} and R_{p2} denote regions of positive vorticity. The two wings are initially clapped together and rotate apart along their trailing edges. This rotation creates two large leading edge vortices. Towards the end of rotation, the wings begin to translate apart. During translation, two weak trailing edge vortices begin to form. In this diagram, the wings are moving away from each other at a constant speed and angle of attack. The leading edge vortices (denoted by R_{n1} and R_{p1}) are stronger than the trailing edge vortices (denoted by R_{n2} and R_{p2}). This vortical asymmetry results in larger lift forces than in the symmetrical case without fling.

that follows a clap half-stroke. The force coefficients were averaged over wing rotation and subsequent translation of about 3.5 chord lengths. For all Re considered, lift and drag coefficients were higher for fling half-strokes that followed clap half-strokes. This ‘wake effect’ decreases with decreasing Re .

Discussion

The main result of this paper is that the lift-enhancing effects of clap and fling are larger for lower Re than for higher Re . Not only are large lift forces generated during wing rotation, but they are also transiently enhanced during the translation of the wing following fling. This can be shown by comparing the lift forces generated by two wings to one wing performing the same motion. In practice, the part of the translational phase during which lift is enhanced lasts long enough to comprise most or all of the actual wing motion. For $Re=64$ and higher, clap and fling enhances lift during wing rotation, but does not enhance lift significantly during translation. For $Re=32$ and below, lift is significantly enhanced following clap and fling when compared to the one-winged case. This lift-enhancing effect increases with decreasing Re . Moreover, these Re differences in lift enhancement could explain why most tiny insects have converged upon clap and fling while the vast majority of larger insects do not use this mechanism.

Another result of potential significance is that the relative drag forces required to rotate the wings apart during fling increase drastically for lower Re . In these simulations, the wings begin fling at a distance of 1/6 chord lengths apart. In reality, the wings are pressed together, and it is reasonable to assume that the drag forces generated during fling would be even greater.

Some of the difference between the higher and lower Re cases can be related to an aerodynamic transition observed in this Re range (Childress and Dudley, 2004; Vandenberghe et al., 2004; Miller and Peskin, 2004). For $Re=64$ and above in three-dimensional strokes, lift is generated in part when an attached leading edge vortex is formed and a trailing edge vortex is shed during each wing stroke. This vortical asymmetry generates negative circulation around the wing and, consequently, creates positive lift. Lift is also produced similarly in two-dimensional simulations at higher Re . However, the leading edge vortex is only transiently attached to the wing. At these high Re , lift enhancement by clap and fling during translation is minimal (at least in two dimensions). For $Re=32$ and below in two dimensions, leading and trailing edge vortices form and remain attached to the wing during each stroke. This vortical symmetry greatly reduces the circulation around the wing and the lift produced when compared to the three-dimensional case of flight at higher Re . A recent study by Wu and Sun (2004) also suggests that lift is greatly reduced at these lower Re in three dimensions. During clap and fling, two large attached leading edge vortices are formed on each wing, and no trailing edge vortices are formed initially. When the wings begin to translate away from one another, two weak trailing edge vortices are formed on each wing and grow during translation. The leading edge vortices, however, are much

stronger than the trailing edge vortices throughout the stroke. This vortical asymmetry produced by clap and fling recovers some of the lift lost from this transition.

To understand the aerodynamic mechanism of lift generation, consider the case of fling shown in Fig. 21. The two wings were rotated apart along their trailing edges and are now translating away from each other along a horizontal plane. By convention, positive motion is defined from right to left so that the circulation around the left wing is negative and the lift is positive. During rotation, two large leading edge vortices (\mathbf{R}_{n1} and \mathbf{R}_{p1}) of equal strength and opposite sign were formed and remain attached to the wing. During translation, two small trailing edge vortices of equal strength and opposite sign begin to form and grow in strength (\mathbf{R}_{n2} and \mathbf{R}_{p2}). Let the rest of the fluid domain (\mathbf{R}_f) be of negligible vorticity. Note that the subscript \mathbf{n} denotes regions of negative (clockwise) vorticity, and \mathbf{p} denotes regions of positive (counterclockwise) vorticity. In the following discussion, an Eulerian frame of reference will be used. The total lift acting on both wings can then be defined as follows using a general viscous aerodynamic theory developed by Wu (1981):

$$F_L = \rho \frac{d}{dt} \iint_{\mathbf{R}_f} x\omega dx dy = \rho \frac{d}{dt} \iint_{\mathbf{R}_{p1}+\mathbf{R}_{p2}} x|\omega| dx dy - \rho \frac{d}{dt} \iint_{\mathbf{R}_{n1}+\mathbf{R}_{n2}} x|\omega| dx dy, \quad (19)$$

where $|\omega|$ is the absolute value of the vorticity. The vortices in each pair are convected in opposite directions with each wing as the wings are translated apart. In an Eulerian framework, the vortices defined by \mathbf{R}_{n1} and \mathbf{R}_{p2} move with negative velocity (the vortices are pulled leftward with the wing). The vortices defined by \mathbf{R}_{p1} and \mathbf{R}_{n2} move with positive velocity (the vortices are pulled rightward with the wing). The equation for total lift in this case can be rewritten as follows:

$$F_L = \rho \left(\left| \frac{d}{dt} \iint_{\mathbf{R}_{n1}} x|\omega| dx dy \right| + \left| \frac{d}{dt} \iint_{\mathbf{R}_{p1}} x|\omega| dx dy \right| \right) - \rho \left(\left| \frac{d}{dt} \iint_{\mathbf{R}_{n2}} x|\omega| dx dy \right| + \left| \frac{d}{dt} \iint_{\mathbf{R}_{p2}} x|\omega| dx dy \right| \right). \quad (20)$$

This equation basically states that the total lift on both wings is proportional to the difference between the magnitude of the time rate of change of the first moment of vorticity associated with the leading edge vorticity and the time rate of change of the first moment of trailing edge vorticity. Therefore, vortical asymmetry produced by clap and fling will transiently enhance lift forces during translation.

List of symbols

A_o	stroke amplitude
c	chord length of wing
c_{targ}	damping coefficient
C_D	drag coefficient
C_L	lift coefficient

f	flapping frequency
$\mathbf{f}(r,t)$	force per unit length applied by the wing to the fluid
\mathbf{f}_{beam}	force per unit length applied to fluid due to bending stiffness
\mathbf{f}_{str}	force per unit length applied to fluid due to stretching stiffness
\mathbf{f}_{targ}	force per unit length applied to fluid due to the target boundary
$\mathbf{F}(\mathbf{x},t)$	total force per unit area applied to the fluid
F_D	drag force
F_L	lift force
F_{scaled}	scaled lift force
k_{beam}	bending stiffness coefficient
k_{str}	stiffness coefficient in tension/compression
k_{targ}	stiffness coefficient of target boundary
l	characteristic length
$P(\mathbf{x},t)$	fluid pressure
r	Lagrangian position
\mathbf{R}_f	two-dimensional fluid space
\mathbf{R}_n	region of negative vorticity
\mathbf{R}_p	region of positive vorticity
S	characteristic surface area
t	time
$\mathbf{u}(\mathbf{x},t)$	fluid velocity
U	characteristic speed
U_{max}	maximum velocity during rotation at the wing's midpoint
$\mathbf{U}(\mathbf{x},t)$	velocity of the boundary
$v(\tau)$	translational velocity at dimensionless time ?
V	maximum translational velocity
\mathbf{x}	position vector
$x(t)$	horizontal position of the center of the wing
$\mathbf{X}(r,t)$	position vector of boundary at Lagrangian position r
$\mathbf{Y}(r,t)$	position vector of target boundary at Lagrangian position r
α	angle of attack
β	parameter to set change in angle of attack
$\delta(\mathbf{x})$	delta function
$\Delta\theta$	total angle through which rotation occurs
$\Delta\tau_{\text{accel}}$	dimensionless duration of translational acceleration
$\Delta\tau_{\text{decel}}$	dimensionless duration of translational deceleration
$\Delta\tau_{\text{rot}}$	dimensionless duration of rotational phase
θ	angle between wing and positive x -axis
μ	dynamic viscosity
ν	kinematic viscosity
ρ	fluid density
τ	dimensionless time
τ_{accel}	dimensionless time when translational acceleration begins
τ_{decel}	dimensionless time when translational deceleration begins
τ_{turn}	dimensionless time when wing rotation begins
ϕ	parameter for the timing of wing rotation
Φ	angle between two wings
ω	vorticity
$ \omega $	absolute value of vorticity

$\omega(\tau)$	angular velocity at dimensionless time ?
ω_{rot}	rotational constant
ϕ	parameter to set timing of rotation

We wish to thank Michael Shelley, Stephen Childress and Michael Dickinson for their perceptive comments on our work. We also thank the reviewers for their excellent suggestions which have led to a greatly improved paper. This work was supported by the National Science Foundation under Grant Number DMS-9980069.

References

- Birch, J. M., Dickson, W. B. and Dickinson, M. H.** (2004). Force production and flow structure of the leading edge vortex on flapping wings at high and low Reynolds numbers. *J. Exp. Biol.* **207**, 1063-1072.
- Childress, S. and Dudley, R.** (2004). Transition from ciliary to flapping mode in a swimming mollusc: Flapping flight as a bifurcation in Re_ω . *J. Fluid. Mech.* **498**, 257-288.
- Dickinson, M. H.** (1994). The effects of wing rotation on unsteady aerodynamic performance at low Reynolds numbers. *J. Exp. Biol.* **192**, 179-206.
- Dickinson, M. H. and Götz, K. G.** (1993). Unsteady aerodynamic performance of model wings at low Reynolds numbers. *J. Exp. Biol.* **174**, 45-64.
- Ellington, C. P.** (1984). The aerodynamics of hovering insect flight. III. Kinematics. *Phil. Trans. R. Soc. Lond. B* **305**, 41-78.
- Ellington, C. P.** (1999). The novel aerodynamics of insect flight: Applications to micro-air vehicles. *J. Exp. Biol.* **202**, 3439-3448.
- Hausling, H. J.** (1979). Boundary fitted coordinates for accurate numerical solution of multibody flow problems. *J. Comp. Physiol.* **30**, 107-124.
- Lai, M.-C. and Peskin, C. S.** (2000). An immersed boundary method with formal second order accuracy and reduced numerical viscosity. *J. Comp. Physiol.* **160**, 705-719.
- Lighthill, M. J.** (1973). On the Weis-Fogh mechanism of lift generation. *J. Fluid. Mech.* **60**, 1-17.
- Maxworthy, T.** (1979). Experiments on the Weis-Fogh mechanism of lift generation by insects in hovering flight. Part I. Dynamics of the 'fling.' *J. Fluid. Mech.* **93**, 47-63.
- Miller, L. A. and Peskin, C. S.** (2004). When vortices stick: An aerodynamic transition in tiny insect flight. *J. Exp. Biol.* **207**, 3073-3088.
- Peskin, C. S.** (2002). The immersed boundary method. *Acta Numerica* **11**, 479-517.
- Peskin, C. S. and McQueen, D. M.** (1996). Fluid dynamics of the heart and its valves. In *Case Studies In Mathematical Modeling – Ecology, Physiology, and Cell Biology* (ed. H. G. Othmer, F. R. Adler, M. A. Lewis and J. C. Dallon), pp. 309-337. New Jersey: Prentice Hall, Inc.
- Spedding, G. R. and Maxworthy, T.** (1986). The generation of circulation and lift in a rigid two-dimensional fling. *J. Fluid. Mech.* **165**, 247-272.
- Srygley, R. B. and Thomas, A. L. R.** (2002). Unconventional lift-generating mechanisms in free-flying butterflies. *Nature* **420**, 660-664.
- Sun, M. and Yu, X.** (2003). Flow around two airfoils performing fling and subsequent translation and translation and subsequent flap. *Acta Mech. Sinica* **19**, 103-117.
- Sunada, S., Kawachi, K., Watanabe, I. and Azuma, A.** (1993). Fundamental analysis of three-dimensional 'near fling.' *J. Exp. Biol.* **183**, 217-248.
- Usherwood, J. R. and Ellington, C. P.** (2002). The aerodynamics of revolving wings I. Model hawkmoth wings. *J. Exp. Biol.* **205**, 1547-1564.
- Vandenberghe, N., Zhang, J. and Childress, S.** (2004). Symmetry breaking leads to forward flapping flight. *J. Fluid. Mech.* **506**, 147-155.
- Wang, Z., Birch, J. M. and Dickinson, M. H.** (2004). Unsteady forces and flows in low Reynolds number hovering flight: two-dimensional computations vs. robotic wing experiments. *J. Exp. Biol.* **207**, 449-460.
- Weis-Fogh, T.** (1973). Quick estimates of flight fitness in hovering animals, including novel mechanisms for lift production. *J. Exp. Biol.* **59**, 169-230.
- Weis-Fogh, T.** (1975). Unusual mechanisms for the generation of lift in flying animals. *Sci. Am.* **233**, 80-87.
- Wu, J. C.** (1981). Theory for aerodynamic force and moment in viscous flows. *AIAA J.* **19**, 432-441.
- Wu, J. H. and Sun, M.** (2004). Unsteady aerodynamic forces of a flapping wing. *J. Exp. Biol.* **207**, 1137-1150.